

Precise estimation of the coupling strength between two nanomechanical modes from four Ramsey fringes

Anh Tuan Le,¹ Avishek Chowdhury,¹ Hugo Ribeiro,² and Eva M. Weig^{1, 3, 4}

¹*School of Computation, Information and Technology,*

Technical University of Munich, 85748 Garching, Germany

²*Department of Physics and Applied Physics, University of Massachusetts Lowell, Lowell, MA 01854, USA*

³*TUM Center for Quantum Engineering (ZQE), 85748 Garching, Germany*

⁴*Munich Center for Quantum Science and Technology (MCQST), 80799 Munich, Germany*

We experimentally determine the coupling strength between two strongly coupled nanomechanical modes using a Ramsey-inspired technique optimized for signals as short as four fringes. The method is applied to precisely probe the change of the coupling rate induced by a modification of the microwave-cavity readout field. It opens a pathway towards sensing electrostatic field fluctuations approaching single-charge resolution.

Introduction — Fluctuations in physical and biological systems are an ubiquitous phenomenon that strongly impacts their behavior [1–6]. They govern physical processes, including decoherence [7], and limit the sensitivity of detectors [6]. There is a range of established techniques for their characterization [8–11], which all rely on probing spectral properties. This is sufficient to probe Gaussian noise, the statistics of which is fully determined by its average and its spectrum, i.e. the first and second moment. However, a full characterization of the noise in a system requires, in general, knowledge of all its moments [12]. This is particularly important for non-Gaussian noise, where higher-order moments are required to obtain the full statistics. Probing higher-order moments remains an experimentally outstanding challenge [13–17].

Another, elegant, approach would be to time-resolve the fluctuations directly. This calls for fast and sensitive probes. Time-resolved measurements of fluctuating electromagnetic quantities have been demonstrated [18–21]. These techniques are, however, limited to cryogenic temperatures. Here we present a scheme that allows to time-resolve fluctuations at room temperature. It exploits Ramsey spectroscopy to probe the frequency splitting between the hybridized modes in a nanomechanical two-mode system [22]. Using the recently proposed iterative adaptive spectroscopy protocol [23], the splitting magnitude is accurately obtained from only a small number of Ramsey fringes. We confirm that the splitting depends on the electrostatic environment [24–26]. This opens the way towards investigating non-Gaussian charge fluctuations at room temperature [12], with an estimated single-electron sensitivity and sub-millisecond time resolution.

Nanomechanical two-mode system — The nanomechanical two-mode system is implemented using the two orthogonally polarized fundamental flexural eigenmodes of a nanomechanical string resonator. They are associated with the motion of the resonator along the y and z -axis, vibrating at $\omega_j/(2\pi) \approx 7\text{ MHz}$ where $j \in \{\text{IP, OOP}\}$ for the out-of-plane (OOP) and in-plane (IP) mode, re-

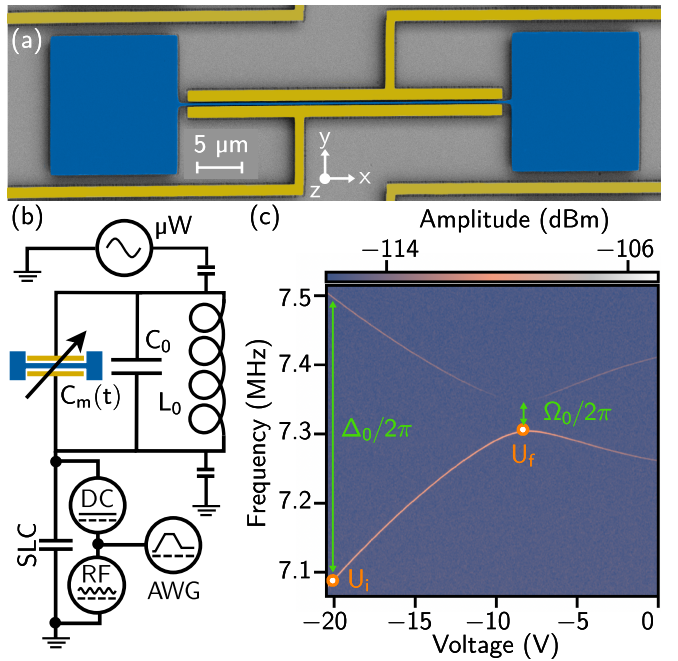


Figure 1. **Experimental realization.** (a) Scanning electron micrograph of a typical silicon nitride string resonator (blue) with the two gold electrodes nearby. (b) Simplified measurement setup. See main text for details. (c) Color plot of amplitude spectra measured as a function of DC voltage, showing an avoided crossing of magnitude Ω_0 between the OOP and the IP mode. The two orange circles denote the DC voltage used for initialization and for tuning on resonance, respectively. Δ_0 is the frequency difference of the two mechanical modes at U_i .

spectively. A typical geometry of the system is shown using a scanning electron micrograph in Fig. 1(a) [see also Appendices A and B]. The $55\text{ }\mu\text{m}$ -long nanostring resonator is made of strongly pre-stressed silicon nitride, and exhibits quality factors in the range of 250,000 at room temperature and 10^{-4} mbar. The resonator is flanked by two gold electrodes used for dielectric control. A schematic of the measurement setup is depicted in

Fig. 1(b); a more detailed description is found in Appendices C and D. One of the electrodes is connected to an antenna that couples to a coaxial $\lambda/4$ three-dimensional (3D) microwave cavity (see Appendix C) used for displacement detection [27–29]. The 3D cavity is made of copper, suitable for room-temperature operation. It is driven by a microwave generator (μW) on resonance $\omega_c/(2\pi) \approx 3$ GHz at $P_c = 22$ dBm. In Fig. 1(b), the 3D microwave cavity is represented by a tank circuit with inductor L_0 and capacitor C_0 . The second electrode is wire-bonded to a single layer capacitor (SLC) that provides a microwave ground path [30] while connecting to a self-made voltage combiner adding a DC and a RF signal with the output of an arbitrary waveform generator (AWG).

The mechanical motion periodically modulates the capacitance $C_m(t)$ of the electrodes, inducing sidebands in the cavity response at frequencies $\omega_c \pm \omega_j$ which are demodulated using heterodyne IQ-mixing as described in Appendix D. Application of a DC voltage to the second electrode allows for dielectric tuning of the mechanical eigenfrequencies ω_j [30, 31]. The DC voltage also induces strong dielectric coupling between the IP and OOP mode the magnitude of which is governed by the polarizability of the dielectric material α and the inhomogeneous electric field \mathbf{E} between the electrodes [27] (see also Appendix B). This gives rise to a pronounced avoided level crossing [see Fig. 1 (c)] with a frequency splitting Ω_0 around which both modes hybridize into normal modes. The system can be described as a two-mode system, as all higher-order flexural modes only appear at eigenfrequencies approximately given by $N\omega_j$, corresponding to a quasi-infinite anharmonicity since $\Omega_0/(N\omega_j) \ll 1$ for $N \geq 1$. Combination of the DC voltage with a RF voltage resonant at ω_j dielectrically actuates mode j [31].

Ramsey-based Iterative Adaptive Sensing (IAS) — The straightforward way to measure the normal mode splitting in our system is to perform a spectroscopic noise driven measurement of the resonant frequencies as a function of applied DC voltage [see Fig. 1 (c)] and extract the value of Ω_0 from a fit. The fit function is chosen to match the spectrum of two classically coupled harmonic oscillators [32] (see also Appendix B), which provides a good description of the spectrum in the vicinity of the avoided crossing. However, the robustness of the fit depends heavily on the signal to noise ratio of the measured data and the precise knowledge of several system parameters. Additionally, such spectroscopic measurements are based on parametric sweeps and require long average times, making them unsuitable for sensing applications.

The alternative relies on the observation that at the avoided crossing, the hybridized modes can exchange energy at a rate faster than the characteristic decoherence time T_d of the system. Thus, in the limit $\Omega_0/(2\pi)T_d \ll 1$, the hybridized modes can be coherently controlled, al-

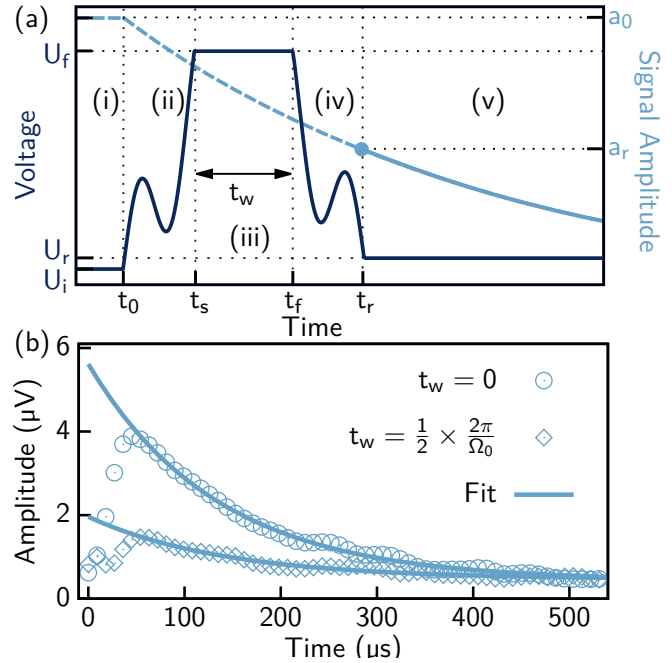


Figure 2. **Implementation of the Ramsey interferometry.** (a) Ramsey pulse sequence with the corresponding first harmonic Magnus-based correction of the leading (ii) and the trailing (iv) edges for frequency-sweep. Note we introduce a finite voltage offset $U_r - U_i \neq 0$ that allows the readout state a_r to decay, whereas the initial state a_i is continuously driven. (b) Ringdown measurement of the IP mode after completing the Ramsey sequence for two different waiting times t_w . The exponential fits extrapolate back to $t_0 = 0$ to compensate the mechanical damping during the evolution time and are used to convert the signal into a return probability [36, 37].

lowing for the implementation of Ramsey spectroscopy-based sensing [22, 33–35].

Applied to our system, it consists of the following steps also visualized in Fig. 2 (see also Appendix E):

- (i) Initialize the IP mode by applying a RF voltage at $\omega_{\text{IP}}(U_i)$ at a DC bias U_i [see Fig. 1 (c)] fulfilling the condition $\Delta_0 = \omega_{\text{OOP}} - \omega_{\text{IP}} \gg \Omega_0$.
- (ii) Using the initial estimate $\bar{\Omega}_0$ of Ω_0 obtained from the spectrum fit, design a non-adiabatic frequency-sweep $\Delta(t)$ that quickly brings the IP mode into the avoided level crossing at a DC bias of U_f with a high-fidelity [see Fig. 2 (a)]. A voltage signal encoding $\Delta(t)$ is generated by an Arbitrary Waveform Generator (AWG) and applied to the system along with the DC and RF voltage [see Fig. 1 (b)]. This prepares the ideal sensing state [23]. In general, the ideal sensing state consists of an equal superposition of the two normal modes. At the avoided crossing, the normal modes vibrate with a polarization of $\pm 45^\circ$ [22, 27]. Here we choose the equal superposition reproducing the IP mode [see Appendix E].

- (iii) Let the system evolve freely for a time $t_w = 2\pi n/\bar{\Omega}_0$, where n is an integer. The coherent evolution allows this state to pick up a phase equal to $\phi = \bar{\Omega}_0 t_w$.
- (iv) Bring the system back to a bias U_r close to the initial bias point U_i by applying the reverse frequency-sweep to $\Delta(t)$ defined in (ii). Ideally, U_r should coincide with U_i . In practice, a finite offset of a few 100 mV is applied to avoid interference with the RF drive voltage [see Fig. 2 (a)].
- (v) Extract the amplitude of the IP mode at U_r from a ringdown measurement as a function of the free evolution time $[0, t_w]$ [see Fig. 2 (b)] and convert it into a return probability [36, 37]. This constitutes the Ramsey signal.

The obtained amplitude as a function of time yields an ideal Ramsey signal with unity visibility ignoring decoherence and assuming perfect knowledge of the splitting $\bar{\Omega}_0$. However the spectroscopic method does not provide that level of accuracy, since it involves a small but non-negligible error in the determination of $\bar{\Omega}_0$, which severely deteriorates the Ramsey signal as described in Ref. [23]. The recently proposed IAS (Iterative Adaptive Spectroscopy) protocol [23] provides a means to bypass both decoherence and the imprecise knowledge of $\bar{\Omega}_0$. At its heart IAS represents an enhanced Ramsey protocol that allows one to precisely extract frequency information from short Ramsey signals consisting only of a small number of fringes n ($n < 10$). It combines an iterative procedure with signal processing to achieve a fast and accurate measurement of the frequency splitting of a two-mode system. Using the spectroscopic guess as a prior estimate of the splitting $\bar{\Omega}_0^{(0)}$, we perform a first Ramsey sequence [(i) - (v)]. A fast Fourier transform of the short Ramsey signal is performed to extract a new estimate $\bar{\Omega}_0^{(1)}$. This constitutes the starting point of IAS. Using $\bar{\Omega}_0^{(1)}$, all input parameters of the Ramsey sequence are updated before proceeding to the next iteration $m = 2$ (see Appendix F). To avoid known issues linked to Fourier transforms of short signals, IAS relies on signal processing (windowing and zero-padding) as described in [23]. This procedure is repeated until the frequency estimate $\bar{\Omega}_0^{(m)}$ saturates.

Here, we experimentally apply the IAS protocol to the classical nanomechanical two-mode system [22, 32, 36–38] to sense charge fluctuations building up on the surface of the nanomechanical resonator. Notice that all data shown in the following has been obtained after averaging over 30 measurements.

Precision frequency sensing with IAS — To illustrate the shortcomings of a standard Ramsey sequence, we measure the return probability of a non-iterated sequence over $n = 2$ fringes. The black data in Fig. 3 (a) and (b) depicts the Ramsey time trace as well as its fast Fourier

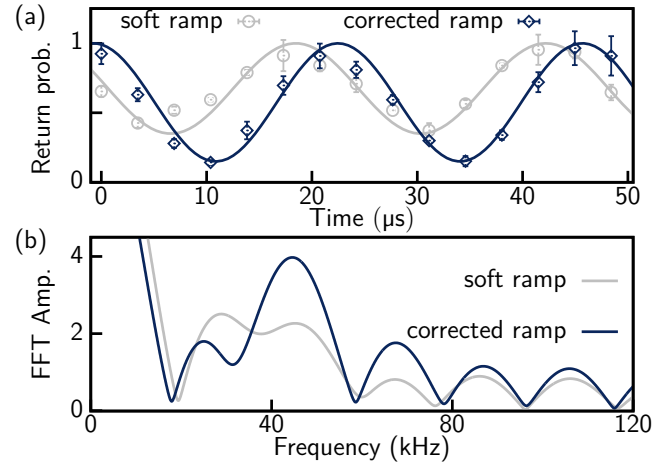


Figure 3. **State preparation.** (a) Ramsey signal (return probability of the state a_i) for two different initialization protocols. Measurement time captures approximately 2 periods. Data has been averaged over 30 measurements. Grey (blue) datapoints bar are obtained with a sinusoidal soft ramp (corrected ramp, c.f. 2). Solid grey (blue) lines indicate fits. (b) Fast Fourier transform of the short, zero-padded Ramsey signals. Grey (blue) line corresponds to the initialization via the soft (corrected) ramp, respectively.

transform (FFT) for the case of a fast frequency sweep consisting of a simple cosine-shaped soft ramp [23]. The two apparent Ramsey fringes exhibit a poor visibility of only approximately 60 %, and the FFT does not reveal a clear maximum indicative of the splitting $\bar{\Omega}_0$. The apparent double peak is an artefact from the intense side lobes arising from finite-time effects (spectral leakage) [23]. Note that “maximum” refers to a local maximum, excluding the zero-frequency peak. We will employ this convention throughout. The blue data in Fig. 3 (a) and (b) was measured for an improved frequency sweep based on a first harmonic Magnus-based correction [see Fig. 2 (a)]. The visibility of the Ramsey fringes for the corrected ramp is significantly improved to about 85 %, and the FFT yields a clear maximum at $\bar{\Omega}_0^{(1)}$. This is close to optimal, since the calculation of the corrected pulse relies on the inaccurate prior estimate $\bar{\Omega}_0^{(0)} = 41.3$ kHz (see Supplemental Material B). In addition, the spectral leakage still distorts the spectrum, preventing to reliably extract the maximum. Notice that both traces extend slightly beyond the second Ramsey fringe. This is also a consequence of the discrepancy between $\bar{\Omega}_0^{(0)}$ and $\bar{\Omega}_0$.

The IAS protocol is applied in Fig. 4. It displays a full IAS sequence for up to $m = 12$ iterations. The number of measured Ramsey fringes for $m > 1$ is increased to $n = 4$ in order to apply the IAS signal processing procedure [23]. The extracted splitting $\bar{\Omega}_0^{(m)}$ as a function of the iteration m is shown in Fig. 4 (a). The first datapoint $\bar{\Omega}_0^{(1)}$ is obtained from a FFT of a two-fringe time trace obtained with the corrected ramp like in Fig. 3 (b),

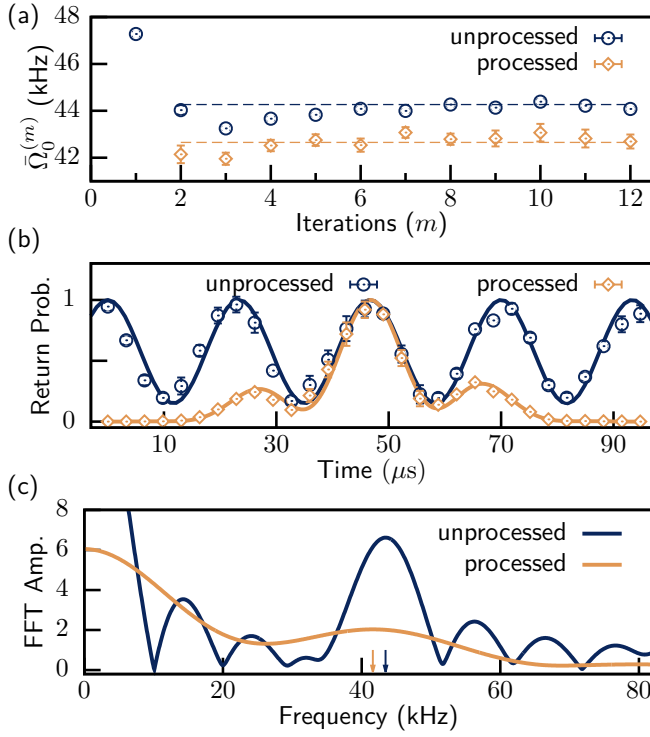


Figure 4. Iterative adaptive spectroscopy for short and finite signals. (a) Frequency estimation for each iteration step m . The $m = 1$ datapoint was obtained from a two-period Ramsey signal as in Fig. 3. Blue (orange) symbols refer to the unprocessed (processed) data. Error bars indicate standard deviation of the 30 measurements. (b) Ramsey signal (return probability of the state a_i) sampling $n = 4$ fringes at $m = 8$ before (blue) and after data processing (orange). (c) Fast Fourier transform of the zero-padded data shown in (b). Orange (blue) arrow marks position of the local maximum indicating frequency estimate $\bar{\Omega}_0^{(8)}$ in (a).

albeit frequencies do not match as both traces have been obtained for different sample conditions [39]. The extracted splittings for $m > 1$ are obtained with the IAS procedure described previously (see also [23]). For each iteration, we compare the frequency splitting obtained before (blue datapoints, in the following referred to as unprocessed data) and after applying the windowing (yellow datapoints, processed data). Notably, the data converges quickly to $\bar{\Omega}_0^{(\infty)} / (2\pi) = (42.65 \pm 0.35)$ kHz, obtained after averaging all $\bar{\Omega}_0^{(m)}$ for $m \geq 2$. Figure 4 (b) and (c) display the Ramsey time traces as well as their FFTs for $m = 8$. The four Ramsey fringes are clearly visible in the blue trace of Fig. 4 (b) before the windowing is applied. Their visibility of approximately 85 % remains unchanged compared to Fig. 3 (a).

The IAS is designed to produce a Ramsey signal with an integer multiple of the oscillation period. Hence, the measured time trace comprises exactly 4 fringes, demonstrating that IAS efficiently approaches the real split-

ting Ω_0 . The associated FFT in Fig. 4 (c) shows a clear maximum at (44.27 ± 0.08) kHz, along with pronounced side lobes caused by spectral leakage arising from Fourier transforming the short-time data trace without further signal processing [23]).

The yellow trace in Fig. 4 (b) shows the Ramsey signal after the windowing. The convolution with the window function effectively halves the number of fringes. This explains why the $n = 4$ fringes have to be measured in order to be able to perform a FFT when using signal processing. The associated FFT signal in Fig. 4 (c) contains a clear maximum at $\bar{\Omega}_0^{(8)} / (2\pi) = (42.79 \pm 0.24)$ kHz and does not exhibit any side lobes. Suppressing spectral leakage gives rise to a more precise estimate, at the expense of a slightly increased width of the maximum [40]. Therefore, the slightly lower value of $\bar{\Omega}_0^{(8)}$ extracted from the smaller and broader yellow maximum provides the better estimate of Ω_0 than that obtained from the blue trace. Notice that this is also reflected in the size of the error bars in Fig. 4 (a). The processed yellow data exhibits larger statistical uncertainties but provides the better estimate of Ω_0 .

Field and charge sensing with IAS — In the following, we will discuss the use of IAS to probe modifications in the size of the frequency splitting Ω_0 induced by external perturbations. For a proof-of-concept experiment, we perturb the electric field applied between the electrodes. The perturbation is induced by increasing the microwave cavity pump power P_c from 22 dBm to 22.5 dBm which results in a slight shift of the mechanical eigenfrequencies as well as the frequency splitting (see Appendix G). The resulting change of Ω_0 from the situation discussed in Fig. 4 is determined by repeating the IAS measurement as illustrated in Fig. 5.

Figure 5 (a) summarizes the situation before the perturbation is applied, i.e. at $P_c = 22$ dBm. We show histograms of the statistical frequency distribution of the 30 IAS measurements over $n = 4$ fringes at iteration $m = 8$ and indicate their mean value [as also apparent in Fig. 4 (a)]. The yellow data displays the result of the IAS measurement, which yields $\bar{\Omega}_0^{(8)} / (2\pi) = 42.79$ kHz. For comparison, the blue data illustrates the result of a regular, un-iterated two-period Ramsey experiment. As discussed before, the IAS provides the better estimate of Ω_0 , even though the data is more spread. Notably, the two histograms are well-separated, providing clear evidence for the failure of the standard Ramsey experiment for the case of short signals.

Figure 5 (b) displays the frequency estimate obtained after the perturbation, i.e. $P_c = 22.5$ dBm. According to IAS, here evaluated after iteration $m = 3$, the frequency splitting has increased by 3.435 kHz to $\bar{\Omega}_{0,\text{new}}^{(3)} / (2\pi) = (46.23 \pm 0.19)$ kHz (yellow). This corresponds to an added charge density of 180 C/m³ or an equivalent of 1,400 electrons added to the nanowire (see also Appendix G). The

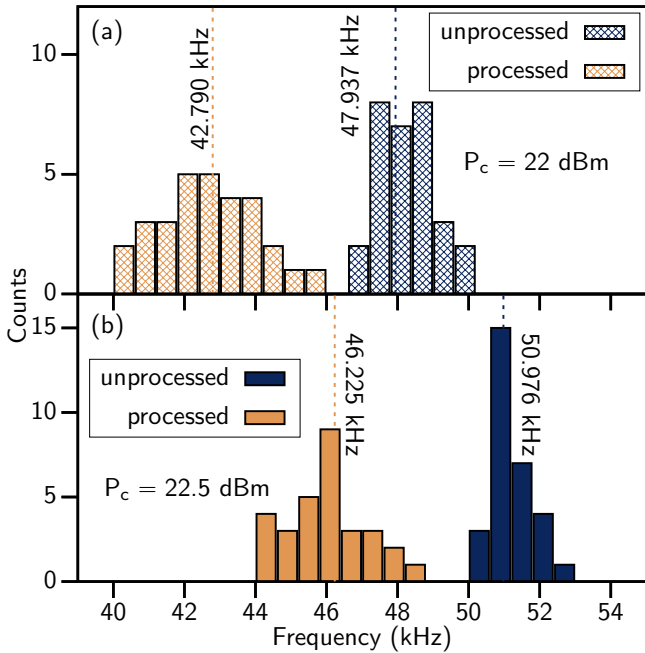


Figure 5. Gradient field sensing. (a) Statistical frequency distributions of 30 Ramsey measurements at iteration $m = 8$ for cavity pump power $P_c = 22$ dBm. Blue and orange bars refer to unprocessed ($n = 2$) and processed ($n = 4$) data, respectively. Dotted lines indicate average $\bar{\Omega}_0^{(8)}$. (b) Statistical frequency distributions of 30 Ramsey measurements after increasing the cavity pump power to $P_c = 22.5$ dBm, probed at iteration $m = 3$.

frequency splitting extracted from the standard, two-period Ramsey experiment also underwent a frequency shift, but of magnitude 3.039 kHz, approximately 12 % off from the correct result. That implies that the two-period Ramsey experiment cannot even be used to extract the relative change of the frequency splitting induced by the perturbation.

In order to validate these findings, we repeat the IAS measurement for while varying the number of Ramsey fringes n . The regular Ramsey experiment is expected to converge to the true Ω_0 for $n \rightarrow \infty$. For the case of IAS, we expect to find the true Ω_0 for a much smaller value of n . Figure 6 shows experimental results for $m = 3$ iterations. As before, the blue and yellow symbols refer to the unprocessed and processed data, respectively. As already discussed in Fig. 4, the unprocessed data for the shortest time-trace of $n = 2$ Ramsey fringes yields a very inaccurate estimation of Ω_0 . For increasing n , the accuracy of the estimate increases, as apparent from the convergence of the extracted frequency near $n = 8$. The shortest time-trace suitable for IAS contains $n = 4$ Ramsey fringes [see Fig. 4 (b)], which already approximates Ω_0 well, within the error margins of the experiment. Not only does this confirm the reliability of the IAS protocol, it also provides a strong justification for trusting the broad IAS

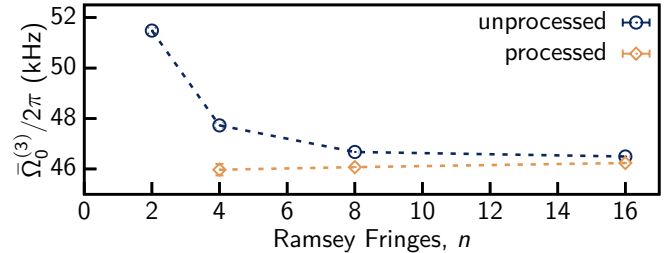


Figure 6. Frequency estimate versus number of Ramsey fringes. Frequency estimation obtained after iteration $m = 3$ as a function of the number of measured Ramsey fringes n at cavity pump power $P_c = 22.5$ dBm. Blue (orange) symbols refer to unprocessed (processed) data, respectively. The unprocessed estimate changes strongly for increasing n , whereas the processed estimate remains nearly constant. For long signals approximating the standard Ramsey measurement ($n \gg 1$), both estimates coincide, validating the IAS approach.

peaks rather than the more narrow unprocessed results in Figs. 4 (a) and 5.

Discussion and outlook — In conclusion, we experimentally demonstrate high-precision frequency estimation from short Ramsey signals comprising only four fringes using a nanomechanical two-mode system. This is accomplished by implementing the recently proposed iterative adaptive spectroscopy (IAS) protocol [23]. We show that IAS converges after four iterations, entailing a significant speedup compared to existing high-precision Ramsey interferometry. In addition, IAS is shown to operate with sparse data sampling approaching the Nyquist sampling rate. A proof-of-principle sensing demonstration reveals a change of the coupling strength subject to perturbations of the electrical field surrounding the nanomechanical string resonator. Exposing the string to an increased microwave cavity field increases the magnitude of the avoided crossing (see Appendix G). Notably, IAS allows a more accurate probe of the resulting change in frequency compared to a standard Ramsey measurement. This holds true both for the net frequency shift and for the relative change induced by the perturbation, implying that the standard Ramsey method is inadequate to measure the induced shift thanks to its limitations for short signals.

We stress that our experimental method is not limited to classical nanomechanical systems but can be applied to any classical or quantum two-level system [34, 35, 41–46]. Its speed of operation suggests IAS as a suitable protocol to study the effect of frequency drifts or fluctuations not accessible with high-resolution Ramsey protocols involving a large number of fringes or even dynamical decoupling strategies. It is equally well-suited for systems with a short coherence time.

Acknowledgements — We acknowledge funding from

the Deutsche Forschungsgemeinschaft (DFG) under Germany's Excellence Strategy—EXC-2111—390814868.

[1] F. J. Giessibl, Advances in atomic force microscopy, *Rev. Mod. Phys.* **75**, 949 (2003).

[2] E. Paladino, Y. M. Galperin, G. Falci, and B. L. Altshuler, $1/f$ noise: Implications for solid-state quantum information, *Rev. Mod. Phys.* **86**, 361 (2014).

[3] L. S. Tsimring, Noise in biology, *Rep. Prog. Phys.* **77**, 026601 (2014).

[4] C. L. Degen, F. Reinhard, and P. Cappellaro, Quantum sensing, *Rev. Mod. Phys.* **89**, 035002 (2017).

[5] L. Pezzè, A. Smerzi, M. K. Oberthaler, R. Schmied, and P. Treutlein, Quantum metrology with nonclassical states of atomic ensembles, *Rev. Mod. Phys.* **90**, 035005 (2018).

[6] A. Bachtold, J. Moser, and M. Dykman, Mesoscopic physics of nanomechanical systems, *Rev. Mod. Phys.* **94**, 045005 (2022).

[7] A. A. Clerk, M. H. Devoret, S. M. Girvin, F. Marquardt, and R. J. Schoelkopf, Introduction to quantum noise and measurement and amplification, *Rev. Mod. Phys.* **82**, 1155 (2010).

[8] Z. A. Maizelis, M. L. Roukes, and M. I. Dykman, Detecting and characterizing frequency fluctuations of vibrational modes, *Phys. Rev. B* **84**, 144301 (2011).

[9] F. Sun, J. Zou, Z. A. Maizelis, and H. B. Chan, Telegraph frequency noise in electromechanical resonators, *Phys. Rev. B* **91**, 174102 (2015).

[10] M. Sansa, E. Sage, E. C. Bullard, M. Gély, T. Alava, E. Colinet, A. K. Naik, L. G. Villanueva, L. Duraffourg, M. L. Roukes, G. Jourdan, and S. Hentz, Frequency fluctuations in silicon nanoresonators, *Nat. Nanotechnol.* **11**, 552 (2016).

[11] X. Wang, X. Wei, D. Pu, and R. Huan, Single-electron detection utilizing coupled nonlinear microresonators, *Microsyst. Nanoeng.* **6**, 78 (2020).

[12] F. Wudarski, Y. Zhang, A. N. Korotkov, A. Petukhov, and M. Dykman, Characterizing low-frequency qubit noise, *Phys. Rev. Appl.* **19**, 064066 (2023).

[13] Gershon, G., Bomze, Yu., Sukhorukov, E. V., Reznikov, and M., Detection of non-gaussian fluctuations in a quantum point contact, *Phys. Rev. Lett.* **101**, 016803 (2008).

[14] B. G. Christensen, C. D. Wilen, A. Opremcak, J. Nelson, F. Schlenker, C. H. Zimonick, L. Faoro, L. B. Ioffe, Y. J. Rosen, J. L. DuBois, B. L. T. Plourde, and R. McDermott, Anomalous charge noise in superconducting qubits, *Phys. Rev. B* **100**, 140503 (2019).

[15] Y. Sung, F. Beaudoin, L. M. Norris, F. Yan, D. K. Kim, J. Y. Qiu, U. von Lüpke, J. L. Yoder, T. P. Orlando, S. Gustavsson, L. Viola, and W. D. Oliver, Non-gaussian noise spectroscopy with a superconducting qubit sensor, *Nat. Commun.* **10**, 3715 (2019).

[16] G. A. L. White, P. Jurcevic, C. D. Hill, and K. Modi, Unifying non-markovian characterization with an efficient and self-consistent framework, *Phys. Rev. X* **15**, 021047 (2025).

[17] J. B. Curtis, A. Yacoby, and E. Demler, Non-gaussian noise magnetometry using local spin qubits, *arXiv:2505.03877* (2025).

[18] R. J. Schoelkopf, P. Wahlgren, A. A. Kozhevnikov, P. Delsing, and D. E. Prober, The radio-frequency single-electron transistor (rf-set): A fast and ultrasensitive electrometer, *Science* **280**, 1238 (1998).

[19] S. Gustavsson, I. Shorubalko, R. Leturcq, T. Ihn, K. Ensslin, and S. Schön, Detecting terahertz current fluctuations in a quantum point contact using a nanowire quantum dot, *Phys. Rev. B* **78**, 035324 (2008).

[20] P. V. Klimov, J. Kelly, Z. Chen, M. Neeley, A. Megrant, B. Burkett, R. Barends, K. Arya, B. Chiaro, Y. Chen, A. Dunsworth, A. Fowler, B. Foxen, C. Gidney, M. Giustina, R. Graff, T. Huang, E. Jeffrey, E. Lucero, J. Y. Mutus, O. Naaman, C. Neill, C. Quintana, P. Roushan, D. Sank, A. Vainsencher, J. Wenner, T. C. White, S. Boixo, R. Babbush, V. N. Smelyanskiy, H. Neven, and J. M. Martinis, Fluctuations of energy-relaxation times in superconducting qubits, *Phys. Rev. Lett.* **121**, 090502 (2018).

[21] H. Bartolomei, E. Frigerio, M. Ruelle, G. Rebora, Y. Jin, U. Gennser, A. Cavanna, E. Baudin, J.-M. Berroir, I. Safi, P. Degiovanni, G. C. Ménard, and G. Fève, Time-resolved sensing of electromagnetic fields with single-electron interferometry, *Nat. Nanotechnol.* **20**, 596 (2025).

[22] T. Faust, J. Rieger, M. J. Seitner, J. P. Kotthaus, and E. M. Weig, Coherent control of a classical nanomechanical two-level system, *Nat. Phys.* **9**, 485 (2013).

[23] A. Chowdhury, A. T. Le, E. M. Weig, and H. Ribeiro, Iterative adaptive spectroscopy of short signals, *Phys. Rev. Lett.* **131**, 050802 (2023).

[24] N. Rossi, F. R. Braakman, D. Cadeddu, D. Vasyukov, G. Tütüncüoglu, A. Fontcuberta i Morral, and M. Poggio, Vectorial scanning force microscopy using a nanowire sensor, *Nat. Nanotechnol.* **12**, 150–155 (2016).

[25] L. M. de Lépinay, B. Pigeau, B. Besga, P. Vincent, P. Poncharal, and O. Arcizet, A universal and ultrasensitive vectorial nanomechanical sensor for imaging 2D force fields, *Nat. Nanotechnol.* **12**, 156 (2017).

[26] F. R. Braakman and M. Poggio, Force sensing with nanowire cantilevers, *Nanotechnology* **30**, 332001 (2019).

[27] T. Faust, J. Rieger, M. J. Seitner, P. Krenn, J. P. Kotthaus, and E. M. Weig, Nonadiabatic dynamics of two strongly coupled nanomechanical resonator modes, *Phys. Rev. Lett.* **109**, 037205 (2012).

[28] M. Reagor, H. Paik, G. Catelani, L. Sun, C. Axline, E. Holland, I. M. Pop, N. A. Masluk, T. Brecht, L. Frunzio, M. H. Devoret, L. Glazman, and R. J. Schoelkopf, Reaching 10 ms single photon lifetimes for superconducting aluminum cavities, *Appl. Phys. Lett.* **102**, 192604 (2013).

[29] A. T. Le, A. Brieussel, and E. M. Weig, Room temperature cavity electromechanics in the sideband-resolved regime, *J. Appl. Phys.* **130**, 014301 (2021).

[30] J. Rieger, T. Faust, M. J. Seitner, J. P. Kotthaus, and E. M. Weig, Frequency and q factor control of nanomechanical resonators, *Appl. Phys. Lett.* **101**, 103110 (2012).

[31] Q. P. Unterreithmeier, E. M. Weig, and J. P. Kotthaus, Universal transduction scheme for nanomechanical systems based on dielectric forces, *Nature* **458**, 1001 (2009).

[32] L. Novotny, Strong coupling, energy splitting, and level crossings: A classical perspective, *Am. J. Phys.* **78**, 1199 (2010).

[33] O. Gittsovich, T. Moroder, A. Asadian, O. Gühne, and P. Rabl, Nonclassicality tests and entanglement witnesses

for macroscopic mechanical superposition states, *Phys. Rev. A* **91**, 022114 (2015).

[34] A. Y. Cleland, E. A. Wollack, and A. H. Safavi-Naeini, Studying phonon coherence with a quantum sensor, *Nature Communications* **15**, 10.1038/s41467-024-48306-0 (2024).

[35] Y. Yang, I. Kladarić, M. Drimmer, U. von Lüpke, D. Lenterman, J. Bus, S. Marti, M. Fadel, and Y. Chu, A mechanical qubit, *Science* **386**, 783 (2024).

[36] M. J. Seitner, H. Ribeiro, J. Kölbl, T. Faust, J. P. Kotthaus, and E. M. Weig, Classical Stückelberg interferometry of a nanomechanical two-mode system, *Phys. Rev. B* **94**, 245406 (2016).

[37] M. J. Seitner, H. Ribeiro, J. Kölbl, T. Faust, and E. M. Weig, Finite-time Stückelberg interferometry with nanomechanical modes, *New J. Phys.* **19**, 033011 (2017).

[38] M. Frimmer and L. Novotny, The classical Bloch equations, *Am. J. Phys.* **82**, 947 (2014).

[39] In the course of the experiment, the vacuum chamber had to be vented which resulted in a shift of eigenfrequencies. The data shown in this manuscript has been obtained after the vent, with the exception of Fig. 3, as the measurement involving the soft ramp was not repeated.

[40] K. M. M. Prabhu, *Window Functions and Their Applications in Signal Processing* (CRC Press, 2018).

[41] J. M. Taylor, P. Cappellaro, L. Childress, L. Jiang, D. Budker, P. R. Hemmer, A. Yacoby, R. Walsworth, and M. D. Lukin, High-sensitivity diamond magnetometer with nanoscale resolution, *Nat. Phys.* **4**, 810 (2008).

[42] D. Ristè, C. C. Bultink, M. J. Tiggelman, R. N. Schouten, K. W. Lehnert, and L. DiCarlo, Millisecond charge-parity fluctuations and induced decoherence in a superconducting transmon qubit, *Nature Communications* **4**, 10.1038/ncomms2936 (2013).

[43] H. Zhou, J. Choi, S. Choi, R. Landig, A. M. Douglas, J. Isoya, F. Jelezko, S. Onoda, H. Sumiya, P. Cappellaro, H. S. Knowles, H. Park, and M. D. Lukin, Quantum metrology with strongly interacting spin systems, *Physical Review X* **10**, 031003 (2020).

[44] M. Hollendonner, S. Sharma, S. K. Parthasarathy, D. B. R. Dasari, A. Finkler, S. V. Kusminskiy, and R. Nagy, Quantum sensing of electric field distributions of liquid electrolytes with nv-centers in nanodiamonds, *New Journal of Physics* **25**, 093008 (2023).

[45] Z. Cheng, X. Ye, J. Wu, P. Yu, C.-J. Wang, M. Wang, C.-K. Duan, Y. Wang, F. Shi, C. Tian, H. Chen, P. Wang, and J. Du, Radio-frequency electric field sensing based on a single solid-state spin, *Physical Review Applied* **19**, 014057 (2023).

[46] K. Capannelli, B. Undseth, I. Fernández de Fuentes, E. Raymenants, F. K. Unseld, O. Pietx-Casas, S. G. J. Philips, M. T. Majdzik, S. V. Amitonov, L. Tryputen, G. Scappucci, and L. M. K. Vandersypen, Tracking spin qubit frequency variations over 912 days, *npj Quantum Information* **11**, 10.1038/s41534-025-01134-6 (2025).

[47] T. Faust, P. Krenn, S. Manus, J. Kotthaus, and E. Weig, Microwave cavity-enhanced transduction for plug and play nanomechanics at room temperature, *Nat. Commun.* **3**, 728 (2012).

[48] A. A. Barakat, A. Chowdhury, A. T. Le, and E. M. Weig, Fundamental and second-subharmonic Autler-Townes splitting in classical systems, *arXiv:2412.16767* (2024).

[49] M. Yuan, V. Singh, Y. M. Blanter, and G. A. Steele, Large cooperativity and microkelvin cooling with a three-dimensional optomechanical cavity, *Nat. Commun.* **6**, 10.1038/ncomms9491 (2015).

[50] A. Noguchi, R. Yamazaki, M. Ataka, H. Fujita, Y. Tabuchi, T. Ishikawa, K. Usami, and Y. Nakamura, Ground state cooling of a quantum electromechanical system with a silicon nitride membrane in a 3d loop-gap cavity, *New Journal of Physics* **18**, 103036 (2016).

[51] N. C. Carvalho, J. Bourhill, M. Goryachev, S. Galliou, and M. E. Tobar, Piezo-optomechanical coupling of a 3d microwave resonator to a bulk acoustic wave crystalline resonator, *Applied Physics Letters* **115**, 211102 (2019).

[52] H. Ribeiro, A. Baksic, and A. A. Clerk, Systematic magnus-based approach for suppressing leakage and nonadiabatic errors in quantum dynamics, *Phys. Rev. X* **7**, 011021 (2017).

[53] T. F. Roque, A. A. Clerk, and H. Ribeiro, Engineering fast high-fidelity quantum operations with constrained interactions, *npj Quant. Inf.* **7**, 28 (2021).

[54] J. Lee, Y. Zhu, and A. Seshia, Room temperature electrometry with sub-10 electron charge resolution, *J. Microeng. Microeng.* **18**, 025033 (2008).

[55] F. Dolde, H. Fedder, M. W. Doherty, T. Nöbauer, F. Rempp, G. Balasubramanian, T. Wolf, F. Reinhard, L. C. L. Hollenberg, F. Jelezko, and J. Wrachtrup, Electric-field sensing using single diamond spins, *Nature Physics* **7**, 459 (2011).

[56] A. Gloppe, P. Verlot, E. Dupont-Ferrier, A. Siria, G. Poncharal, P. and-Bachelier, P. Vincent, and O. Arcizet, Bidimensional nano-optomechanics and topological back-action in a non-conservative radiation force field, *Nat. Nanotechnol.* **9**, 920–926 (2014).

[57] F. R. Braakman, N. Rossi, G. Tütüncüoglu, A. F. i Morral, and M. Poggio, Coherent two-mode dynamics of a nanowire force sensor, *Phys. Rev. Appl.* **9**, 054045 (2018).

[58] F. Fogliano, B. Besga, A. Reigue, L. M. de Lépinay, P. Heringlake, C. Gouriou, E. Eyraud, W. Wernsdorfer, B. Pigeau, and O. Arcizet, Ultrasensitive nano-optomechanical force sensor operated at dilution temperatures, *Nat. Commun.* **12**, 4124 (2021).

Supplemental Material: Precise estimation of the coupling strength between two nanomechanical modes from four Ramsey fringes

Anh Tuan Le,¹ Avishek Chowdhury,¹ Hugo Ribeiro,² and Eva M. Weig^{1,3,4}

¹ School of Computation, Information and Technology, Technical University of Munich, 85748 Garching, Germany

² Department of Physics and Applied Physics, University of Massachusetts Lowell, Lowell, MA 01854, USA

³ TUM Center for Quantum Engineering (ZQE), 85748 Garching, Germany

⁴ Munich Center for Quantum Science and Technology (MCQST), 80799 Munich, Germany

Appendix A: Nanomechanical resonator

The nanomechanical string resonator used in this work is made of strongly pre-stressed stoichiometric silicon nitride LPCVD-deposited on a fused silica substrate. It has dimensions of $w = 250$ nm, $t = 100$ nm and $L = 55$ μ m and is assumed to have simply supported boundary conditions at both clamping points, see Fig. 1 (a).

While its pristine eigenfrequencies can be conveniently obtained from the elastic model of a vibrating string, the situation is getting more complex once the string is exposed to an electrostatic field that induces dielectric forces [30].

Finite Element Method (FEM) simulations are an effective tool to study the behaviour of such complex systems. In our work, we use Comsol Multiphysics to simulate the mechanical properties of the string. This allows to determine the resonant frequency of the in-plane (IP) and out-of-plane (OOP) flexural modes for different electrostatic field configurations by solving the respective eigenvalue problem.

In the absence of any applied voltage, our simulation results reveal that the fundamental resonant frequency of the IP mode is found to be $\omega_{\text{IP}}/(2\pi) = 7.514$ MHz, while the OOP mode is $\omega_{\text{OOP}}/(2\pi) = 7.256$ MHz. The results were obtained through the careful selection of the appropriate material properties, boundary conditions and mesh refinement. Note that these frequencies do not exactly coincide with those measured at a DC voltage of 0 V, as a result of the additional dielectric effects of the RMS average of the microwave readout tone [30]. The displacement profiles of the IP and OOP flexural modes are illustrated in Figs. S1a and S1b, respectively.

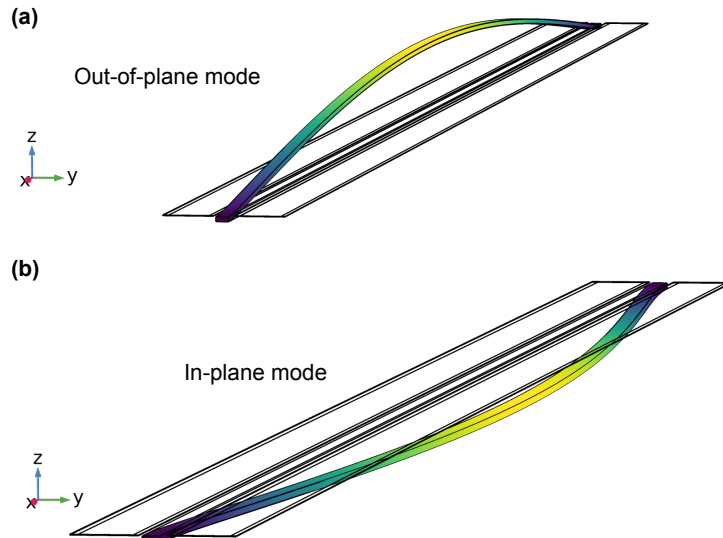


Figure S1. **Vibrational modes of a nanomechanical string resonator.** Comsol Multiphysics 3D simulations illustrate the fundamental displacement profiles of a doubly clamped nanomechanical string resonator that supports out-of-plane (a) and in-plane (b) flexural modes.

Appendix B: Coupled harmonic oscillators

The dynamics of the OOP and IP mode follow the equation of motion of two linearly coupled harmonic oscillators

$$\begin{aligned} m\ddot{u}_1(t) + m\omega_1^2 u_1(t) + \kappa [u_1(t) - u_2(t)] &= 0, \\ m\ddot{u}_2(t) + m\omega_2^2 u_2(t) + \kappa [u_2(t) - u_1(t)] &= 0, \end{aligned} \quad (\text{B1})$$

where u_1 and u_2 describe the displacement of the OOP and IP mode, respectively [32]. The associated angular frequencies of the uncoupled modes are denoted by ω_j ($j = 1, 2$), and κ is the spring coupling constant between the two modes. In our case, the coupling is dielectrically induced [47, 48]. The effective mass of both modes $m = m_{\text{OOP}} = m_{\text{IP}} = \rho L w t / 2$ are equal for a nanostring. For the sake of simplicity we neglect damping.

The eigenfrequencies of the two normal modes can be found by substituting the ansatz $u_j(t) = u_{0,j} \exp(-i\omega t)$ in Eq. (B1). This leads to a system of linear equations for the amplitudes $u_{0,j}$ ($j = 1, 2$) that admit non-trivial solution when $\omega = \omega_{\pm}$. We find

$$\omega_{\pm}^2 = \frac{\omega_1^2 + \omega_2^2 + 2\omega_{\kappa}^2 \pm \sqrt{(\omega_1^2 - \omega_2^2)^2 + 4\omega_{\kappa}^4}}{2}, \quad (\text{B2})$$

where we have defined $\omega_{\kappa} = \sqrt{\kappa/m}$. From Eq. (B2), we can find the minimal level splitting Ω_0 , which corresponds to the frequency splitting when $\omega_1 = \omega_2$. We have

$$\omega_+^2 - \omega_-^2 = (\omega_+ - \omega_-)(\omega_+ + \omega_-) = \sqrt{(\omega_1^2 - \omega_2^2)^2 + 4\omega_{\kappa}^4}, \quad (\text{B3})$$

which leads to

$$\omega_+ - \omega_- = \frac{\sqrt{(\omega_1^2 - \omega_2^2)^2 + 4\omega_{\kappa}^4}}{\omega_+ + \omega_-}. \quad (\text{B4})$$

Assuming $k_1, k_2 \gg \kappa$, and setting $\omega_1 = \omega_2$ in Eq. (B4), we find that the minimal level splitting is given by

$$\Omega_0 \simeq \frac{\omega_{\kappa}^2}{\omega_1} = \frac{\omega_{\kappa}^2}{\sqrt{\omega_1 \omega_2}}. \quad (\text{B5})$$

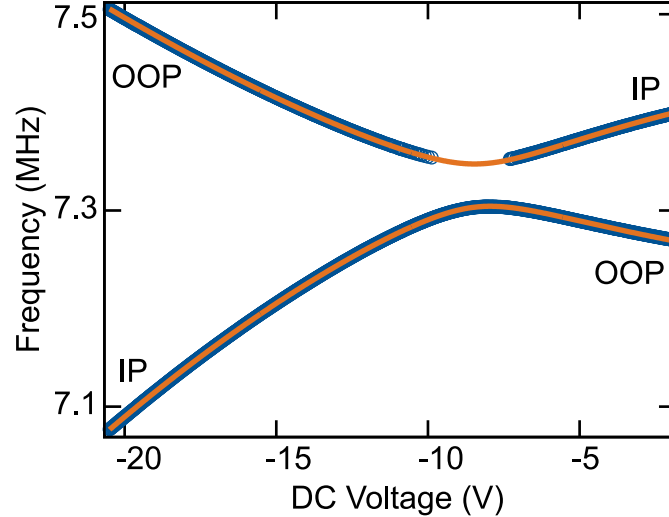


Figure S2. **Avoided Crossing.** Dielectric frequency tuning of the in-plane (IP) and out-of-plane (OOP) mode of the nanostring resonator. Blue circles indicate the eigenfrequencies obtained from Lorentzian fits of the spectroscopic measurement depicted in Fig. 1 (c) of the main text. Orange lines show the fit using Eq. (B2).

Substituting Eq. (B5) in Eq. (B2) allows us to express ω_{\pm} as a function of the measurable frequency Ω_0 . We find

$$\omega_{\pm}^2 = \frac{\omega_1^2 + \omega_2^2 + 2\Omega_0 \sqrt{\omega_1 \omega_2} \pm \sqrt{(\omega_1^2 - \omega_2^2)^2 + 4\Omega_0^2 \omega_1 \omega_2}}{2}. \quad (\text{B6})$$

Changing the DC voltage applied between the electrodes allows tuning the eigenfrequencies [30]. This allows one to map out the avoided crossing between the modes, see Fig. S2. Note the missing data in the upper branch in the region of the avoided crossing. The low visibility in the spectroscopic measurement [see Fig. 1 (c)] hinders the direct extraction of the respective eigenfrequencies. Fitting the above model [see Eq. (B6)] to the data (orange line) reveals a splitting of 41.3 kHz. This value is used as the prior estimate for $\Omega_0/(2\pi)$.

Appendix C: 3D microwave cavity-assisted detection scheme for nanomechanical string resonators

All measurements described in this work have been conducted using the 3D microwave cavity-assisted detection scheme illustrated in Fig. S3. It relies on a coaxial $\lambda/4$ microwave cavity [28]. This type of cavity consists of a narrow cylindrical waveguide with an inner conductor of length l that is shorted-circuited on one end and open on the other. To date, this type of cavity has only been realized at cryogenic temperatures for circuit cavity electrodynamics with superconducting circuits [28], while other types of superconducting 3D cavities have already been adapted for cavity electromechanics [49–51]. Here we use a coaxial $\lambda/4$ cavity made of copper, suitable for room-temperature operation. Thanks to its clean, single mode-like spectrum and its large quality factor, it is better suited for nanomechanical displacement detection than the planar PCB-based [22] or 3D cylindrical cavity [29] employed in previous room-temperature experiments. Our cavity exhibits a waveguide radius and length of 8 mm and 40 mm, respectively, and an inner conductor of radius and length of 1.8 mm and $l = 18$ mm, respectively. The eigenfrequency of the fundamental TEM mode ω_c is defined by the length of the inner conductor $l \approx \lambda/4$. In our case, we find $\omega_c/(2\pi) \approx 3.7$ GHz for the bare cavity, and $\omega_c/(2\pi) \approx 3.0$ GHz for the cavity loaded with the antenna and the sample holder. All other modes of the cavity, including the second harmonic TEM mode as well as the cylindrical waveguide mode TE_{11} , are found at frequencies above 10 GHz. The cavity is pumped on resonance to avoid effects of dynamical backaction on the nanostring resonator.

The nanomechanical string resonator is coupled to the cavity via a microwave antenna that is wire-bonded to one of the gold electrodes. The second gold electrode serves as a microwave ground (see Appendix D). The presence of the antenna and the sample holder leads to a reduction of the cavity eigenfrequency to $\omega_c \approx 3$ GHz. As described in the main text, the mechanical motion at eigenfrequency ω_j ($j \in \{OOP, IP\}$) periodically modulates the capacitance of the electrodes. For the resonantly pumped cavity, this induces sidebands in the cavity response at frequency $\omega_c \pm \omega_j$, which are recorded via the cavity transmission.

The dynamics of the string is controlled via the dielectric drive and control signal, which is also applied via the second gold electrode. It consists of a drive tone (RF), an arbitrary waveform to implement the corrected ramp required for IAS (AWG), as well as the DC voltage. More details about the dielectric drive and control scheme, as well as the demodulation about the microwave signal can be found in Appendix D as well as in Fig. 1 (b) of main text.

Appendix D: Experimental Setup

Figure S4 illustrates the full circuit diagram of the experimental setup. A microwave drive tone from the signal generator (μ W, R&S SMB100) is split into two arms. The first arm pumps the 3D microwave coaxial $\lambda/4$ cavity on resonance at frequency $\omega_c/(2\pi) \approx 3$ GHz to avoid optomechanical backaction effects. The cavity is represented by its L - C equivalent circuit along with the antenna capacitance C_{Ant} (blue-shaded box) coupling the cavity to one of the gold electrodes as described in Appendix C. The second gold electrode provides a ground for the microwave signal via a single layer capacitor (SLC). The mechanical motion of the nanostring periodically modulates the capacitance $C_m(t)$ between the electrodes. This results in a phase modulation of the cavity output signal and imprints sidebands at $\omega_c \pm \omega_j$ onto the cavity response. These are demodulated by mixing the cavity transmission with the reference arm using an IQ-mixer (green-shaded box). The demodulated quadratures are subsequently combined using a $0^\circ/90^\circ$ power splitter [47] (also included in green-shaded box). After filtering out the frequency component at ω_j and amplification of the signal, the amplitude and phase of the mechanical signal is recorded with a spectrum analyzer (SA, R&S FSV). The arbitrary waveform generator (AWG, Keysight 81150A) provides a trigger signal to start the measurements. All devices are synchronized to its internal 10 MHz clock.

Dielectric actuation and control of the nanomechanical resonator is achieved by applying a voltage control signal to the second gold electrode via the SLC [30, 31].

- For the case of a simple spectroscopic characterization as in Fig. 1 (c), the voltage control signal consists of a

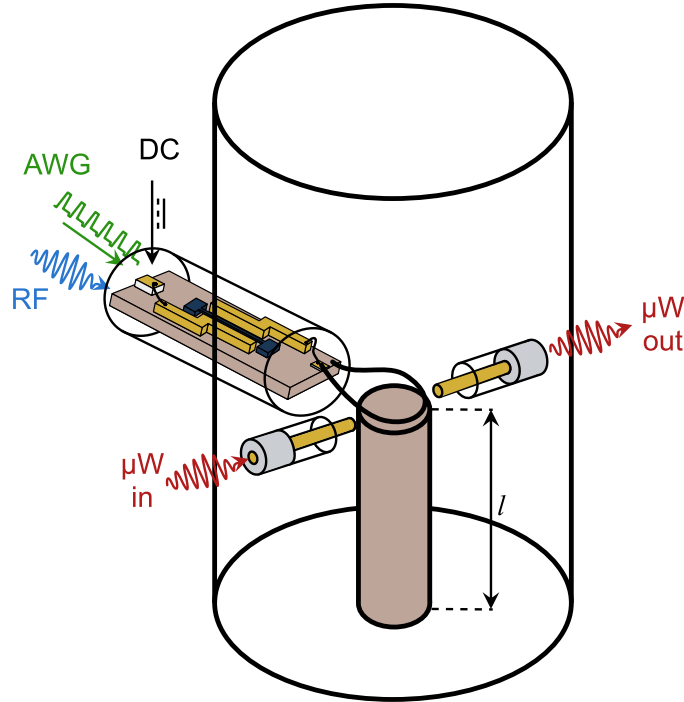


Figure S3. **Coaxial $\lambda/4$ microwave cavity.** Schematic of the 3D microwave cavity and coupling architecture used for dielectric displacement detection of the nanostring.

DC voltage and an RF drive tone. These signals can be conveniently added using a conventional bias tee.

- For the case of IAS, the voltage control signal comprises the DC voltage (DC Source, Keithley 2410), an RF drive tone from a function generator in the MHz regime (RF, Keysight 33500B), and an arbitrary waveform (AWG, Keysight 81150A) providing the voltage ramps. The latter consists of multiple frequency components in the kHz range. This signal cannot be added with a regular bias tee, as its components neither obey the high-frequency cutoff of its DC, nor the low-frequency cutoff of the RF path. To avoid unfaithful pulse generation resulting from bandwidth limitations of the bias tee, we chose a different voltage combination approach based on a series connection of the DC voltage sources and the ramp signal provided by the AWG.

This is implemented in a home-built voltage combiner box (red-shaded box), shown in more detail in Fig. S5 (a). The high impedance nanomechanical string resonator flanked by the two gold electrodes is represented by the circuit elements in the green dashed box. The AWG ramp signal V_1 and the DC voltage V_3 are connected in series. Proper grounding through the box is ensured by floating the DC source.

The RF drive tone V_2 from the function generator is added to the DC-offset AWG signal via a $1\text{ k}\Omega$ impedance. This results in a strong attenuation of V_2 , ensuring operation of the nanostring in the linear response regime, and also provides some isolation.

In Fig. S5 (b), we plot the transmission of the AWG's output voltage V_1 as a function of frequency in a Bode diagram. At low frequencies, a constant transmission close to 0 dB is obtained. The near-negligible attenuation of approximately -0.4 dB results from the minimal loading thanks to the large difference in the output impedances in the two paths (50Ω vs. $1\text{ k}\Omega$). The transmission starts decreasing at frequencies exceeding 100 kHz . This shows that the voltage combiner box allows adding AWG signals with a bandwidth of up to approximately 100 kHz , a significant improvement compared to a standard bias tee.

In the present work, two different types of voltage ramps are employed:

- The soft ramp is implemented demanding $\Omega_0 t_s / (2\pi) = 1/2$, as discussed in detail in Ref. [23]. This corresponds to a sinusoidal voltage signal oscillating at 20.8 kHz (corresponding to $t_s = 12\text{ }\mu\text{s}$), well within the bandwidth of the voltage combiner box.

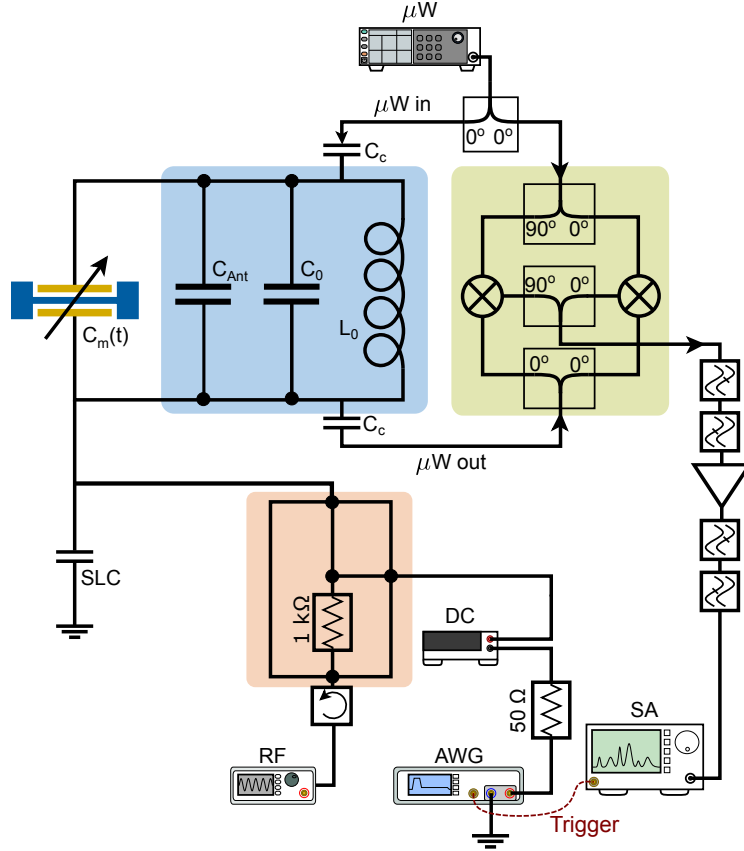


Figure S4. Circuit diagram of the measurement setup. The resonator (blue) with its adjacent electrodes (yellow) are connected to the microwave cavity and the IQ-mixer (shaded in blue and green, respectively) for readout, and to the voltage combiner box (shaded in red) merging the input signals. The single layer capacitor (SLC) provides a capacitive ground for the microwave signal.

- IAS relies on corrected ramps based on the Magnus-based strategy for control. These require higher order frequency components (see Appendix F). For example, the first harmonic Magnus-based correction used in the present work [c.f. Fig. 2 (a)] combines a 20.8 kHz and a 41.6 kHz signal, equally well within the bandwidth of the box.

Notice that higher harmonic Magnus-based corrections involving additional, higher-frequency components, can, in principle, increase the accuracy of the state generation. However, they will get close to or exceed the bandwidth of the voltage combiner box and therefore lead to an unfaithful pulse shape on the sample, and have not been explored in the context of this work.

Appendix E: Ramsey protocol

The Ramsey protocol is a spectroscopic method that allows for the resolution of the frequency splitting between two states. In the following, we will use the ket notation to label the two classical states as $|0\rangle$ and $|1\rangle$. These states are conveniently visualized on a Bloch sphere. In general, the Ramsey sequence consists of a series of five distinct steps:

- The two-level system is prepared in one of the chosen basis states $|0\rangle$ or $|1\rangle$ as a fiducial state.
- A equally-weighted superposition state of the two basis states $|\psi\rangle = (|0\rangle - e^{i\varphi}|1\rangle)/\sqrt{2}$ with an arbitrary phase φ is prepared as the sensing state.

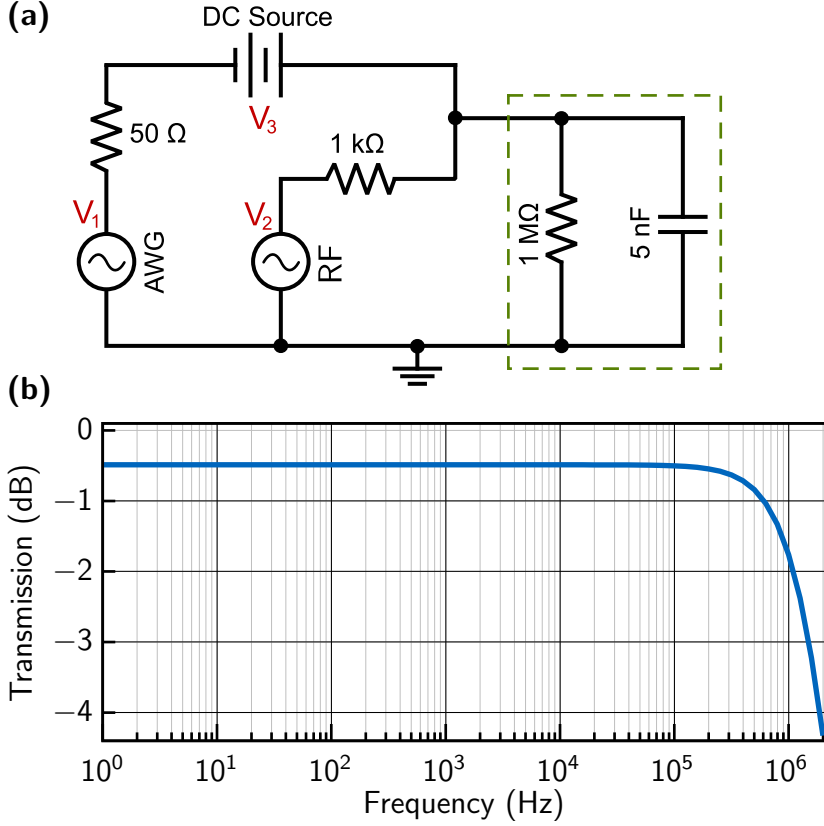


Figure S5. **Voltage combiner box.** (a) Circuit diagram. (b) Bode diagram.

- (III) By letting $|\psi\rangle$ evolve freely for a time t_w , the relative phase between $|0\rangle$ and $|1\rangle$ is evolving, giving rise to a precession of the state in the superposition plane of the Bloch sphere.
- (IV) The final state $|\psi(t_w)\rangle$ is projected back into one of the two original basis states as the readout state.
- (V) The return probability of finding the readout state is measured as a function of t_w .

There are several ways to physically assign the basis states $|0\rangle$ and $|1\rangle$. This is illustrated in Fig. S6, which describes two distinct ways of implementing the Ramsey sequence on a nanomechanical two-mode system.

Figure S6 (a) depicts the energy spectrum of a two-mode system with splitting Ω_0 . It can be thought of as the two nanomechanical modes tuned on resonance (with hybrid normal modes $\not\not$ and $\not\not\not$), but also corresponds to the standard configuration of a spin 1/2 or a qubit. In this case, the normal modes $\not\not$ and $\not\not\not$ are chosen as the basis states. This gives rise to the Ramsey sequence illustrated in Fig. S6 (b), which corresponds to the conventional Ramsey sequence [4].

Its five distinct steps are implemented as follows:

- (I) The two-level system is prepared in its ground state $\not\not$, as depicted in the first Bloch sphere of Fig. S6 (b). For a nanomechanical two-mode system this can be accomplished by slow adiabatic passage which brings the system from one of its uncoupled eigenmodes $\not\not$ or $\not\not\not$ into the avoided level crossing [22].
- (II) The equally-weighted superposition state (sensing state) is generated by applying a resonant $\pi/2$ pulse. It rotates the state into the equatorial plane of the Bloch sphere, as illustrated in the second Bloch sphere of Fig. S6 (b).
- (III) The sensing state precesses in the equatorial plane during time t_w . Notice that for the case of the nanomechanical two-mode system, it will oscillate between the original IP and OOP mode, see third Bloch sphere of Fig. S6 (b).
- (IV) A second $\pi/2$ pulse is used to project the final state back into the readout state $\not\not$, as shown in the fourth Bloch sphere of Fig. S6 (b).

(V) The probability of finding the readout state \Downarrow is measured. This is also illustrated in the fourth Bloch sphere of Fig. S6 (b). For a nanomechanical two-mode system, this is done using a second, reverse adiabatic passage followed by a ringdown measurement of an uncoupled eigenstate (\Downarrow or \Updownarrow) [22].

Figure S6 (c) shows the energy spectrum of a tunable two-mode system. It exhibits an avoided level crossing with splitting Ω_0 which can be addressed by tuning the voltage V . Far from the avoided crossing, the system is best described by its uncoupled eigenstates \Downarrow and \Updownarrow . This is the case as long as their frequency separation greatly exceeds Ω_0 . The Ramsey sequence illustrated in Fig. S6 (d) starts at a particular initialization point where this separation is Δ_0 . For the nanomechanical two-mode system the uncoupled eigenstates correspond to the OOP and IP mode, respectively. When the system is tuned towards the avoided crossing, the uncoupled eigenstates start hybridizing into the normal modes \Downarrow and \Updownarrow . The small Roman numerals indicate the steps of the Ramsey sequence illustrated in Fig. S6 (d) and described in the main text. This Ramsey sequence is best described using the basis of the uncoupled eigenstates \Downarrow , \Updownarrow , which map onto the south and north pole of the Bloch sphere used in Fig. S6 (d). The equatorial plane hosts equal superpositions of the two basis states. On the x-axis of the Bloch sphere, we find $\Updownarrow = (\Downarrow + \Updownarrow)/\sqrt{2}$ and $\Downarrow = (\Downarrow - \Updownarrow)/\sqrt{2}$, recovering the normal modes. This choice of basis gives rise to the Ramsey sequence illustrated in Fig. S6 (d).

Its five distinct steps are implemented as follows (see also [23] for more details):

- (i) The initialization of the system is performed far-detuned from the avoided level crossing [c.f. label (i) in Fig. S6 (c)]. In this configuration, we chose the IP mode \Updownarrow as the initialization state. The energy separation of the two eigenmodes at the initialization point corresponds to $\Delta_0 \ll \Omega_0$. This is reflected in a larger radius of the first Bloch sphere of Fig. S6 (d).
- (ii) To prepare the sensing state, the system is brought into the avoided level crossing using a voltage sweep [c.f. label (ii) in Fig. S6 (c)]. The sensing state represents an equally-weighted superposition state of the two eigenmodes at the avoided crossing, i.e., the normal modes \Updownarrow and \Downarrow . Expressed in the chosen basis, they correspond to $\Updownarrow = (\Updownarrow - \Downarrow)/\sqrt{2}$ and $\Downarrow = (\Updownarrow + \Downarrow)/\sqrt{2}$. So unlike in the conventional Ramsey configuration, the sensing state is oriented *along* the z-axis of the Bloch sphere. Here we chose \Updownarrow as the sensing state. The choice of initialization and sensing state (both \Updownarrow , but at two different bias points, reflected in a modified radius of the Bloch spheres) implies that the voltage sweep must generate an operation proportional to an identity. In principle, this can be realized by an instantaneous voltage sweep. In practice, given the bandwidth limitations of arbitrary waveform generators, such a sweep is impractical. Instead, one can resort to control techniques to realize the desired dynamics. Here, we use the Magnus-based strategy for control to generate an identity operation, see Appendix F for more details.
- (iii) The sensing state precesses in the superposition plane of the normal modes \Updownarrow and \Downarrow . Here this corresponds to the y - z -plane. The state evolves freely during time t_w .
- (iv) A reverse voltage sweep is used to project the final state back into the far-detuned readout state \Updownarrow [c.f. label (iv) in Fig. S6 (c)]. As discussed before, this requires an identity operation. The change in bias point is illustrated in a modified radius of the Bloch sphere. We use the time-reverse of the pulse described in step (ii), c.f. Fig. 2 (a).
- (v) The probability of finding the far-detuned readout state \Updownarrow is measured.

The two Ramsey sequences described in Figs. S6 (b) and (d) both yield a signal which contains spectral information about the splitting Ω_0 . However, the different choice of basis has certain implications: From a mathematical point of view, the signal in the conventional Ramsey sequence, c.f. Figs. S6 (b), is equivalent to measuring the expectation value of the Pauli matrix $\sigma_z = |\Updownarrow\rangle\langle\Updownarrow| - |\Downarrow\rangle\langle\Downarrow|$, whereas the signal in the Ramsey sequence implemented in the present work, c.f. Figs. S6 (d), is equivalent to measuring the expectation value of the Pauli matrix $\sigma_z = |\Downarrow\rangle\langle\Downarrow| - |\Updownarrow\rangle\langle\Updownarrow|$. The two different choices of σ_z are related by a rotation of the Bloch sphere as detailed in the following: The Bloch sphere of interest is obtained from the conventional Bloch sphere by a $-\pi/2$ rotation of the Bloch sphere in Fig. S6 (b) around its y-axis. Correspondingly, the conventional Bloch sphere is recovered from the Bloch sphere in Fig. S6 (d) by a $\pi/2$ rotation around its y-axis. In other words, using the choice of basis and definition of Fig. S6 (b), the Ramsey measurement of Fig. S6 (d) is equivalent to a measurement of σ_x [in the basis of the hybrid modes \Downarrow , \Updownarrow used in Figs. S6 (b)].

For the nanomechanical two-mode system (and for *any* other tunable two-mode system) one can choose to implement either of the two Ramsey sequences. For example, the conventional Ramsey sequence [Figs. S6 (a) and (b)] was used

to demonstrate full Bloch sphere control and Stückelberg interferometry [22, 36, 37]. Here, we opt for the other Ramsey sequence [Figs. S6 (c) and (d)], which allows for a faster initialization. Given that the nanomechanical two-mode system needs to be initialized far from the avoided level crossing to avoid spurious effects of the drive, the implementation of the conventional Ramsey sequence requires a slow adiabatic passage to bring the system from the initialized uncoupled eigenmode ($\uparrow\downarrow$ or $\leftrightarrow\leftrightarrow$) into the avoided level crossing. On the other hand, as detailed in the main text as well as in Appendix F, the initialization for the Ramsey sequence under investigation calls for a fast, non-adiabatic pulse.

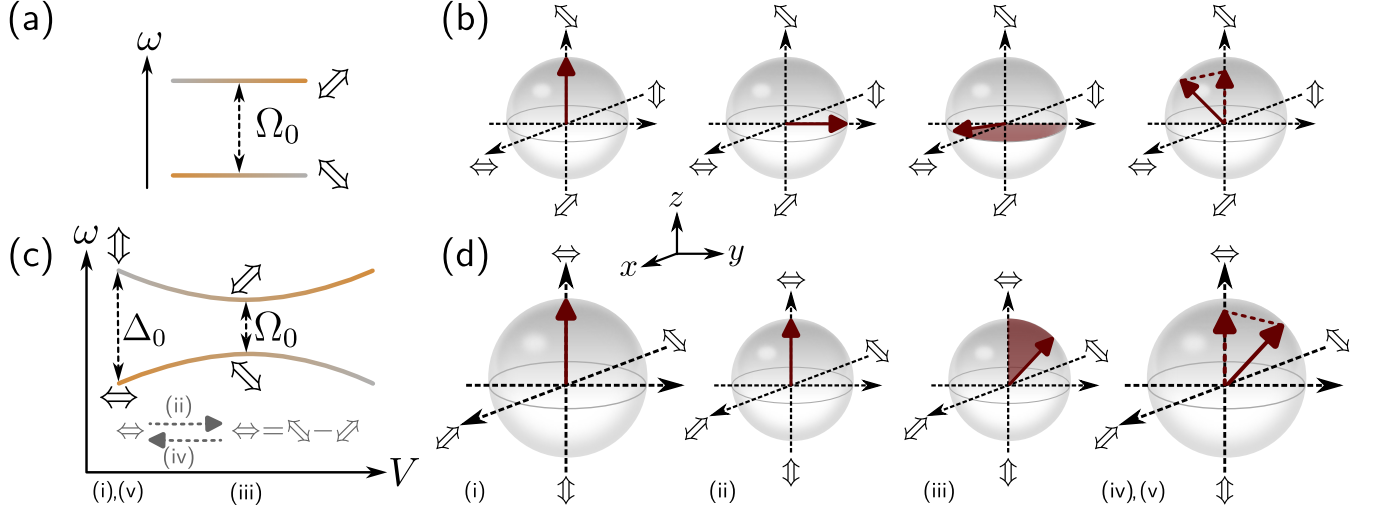


Figure S6. **Comparison of Ramsey protocols.** (a), (b) Ramsey protocol in the basis of normal modes $\uparrow\downarrow$ and $\leftrightarrow\leftrightarrow$. (a) Splitting between the normal modes $\uparrow\downarrow$ and $\leftrightarrow\leftrightarrow$ at the avoided crossing. (b) Definition of Bloch sphere and Ramsey sequence in the basis defined in (a). (c), (d) Ramsey protocol in the basis of uncoupled modes $\uparrow\downarrow$ and $\leftrightarrow\leftrightarrow$. (c) Avoided crossing in the basis uncoupled modes $\uparrow\downarrow$ and $\leftrightarrow\leftrightarrow$, hybridizing into normal modes $\uparrow\downarrow$ and $\leftrightarrow\leftrightarrow$ on resonance. (d) Definition of Bloch sphere and Ramsey sequence in the basis defined in (c). Lower case Roman numerals in (c) and (d) indicate steps of the Ramsey sequence described in the main text.

Appendix F: Nanomechanical implementation of IAS

The dynamics of the IAS protocol is modeled by the Hamiltonian [23]

$$H(t) = \frac{\Delta(t)}{2} \sigma_z + \frac{\Omega_0}{2} \sigma_x, \quad (\text{F1})$$

where σ_x , σ_y and σ_z are the Pauli matrices [with $\sigma_x = |\uparrow\downarrow\rangle\langle\uparrow\downarrow| + |\leftrightarrow\leftrightarrow\rangle\langle\leftrightarrow\leftrightarrow|$, $\sigma_y = -i|\uparrow\downarrow\rangle\langle\uparrow\downarrow| + i|\leftrightarrow\leftrightarrow\rangle\langle\leftrightarrow\leftrightarrow|$, $\sigma_z = |\uparrow\downarrow\rangle\langle\uparrow\downarrow| - |\leftrightarrow\leftrightarrow\rangle\langle\leftrightarrow\leftrightarrow|$, c.f. Appendix E and Figs. S6 (c) and (d)] and $\Delta(t) = \omega_{\text{OOP}}(t) - \omega_{\text{IP}}(t)$ is the frequency difference between the OOP and the IP mode. This quantity is tunable via the applied voltage $U(t)$. For a simple spectroscopic measurement as in Fig. 1 (c), this is implemented by a DC voltage sweep [30, 31], while for the more complex IAS sequence the arbitrary waveform generator is used to generate $\Delta[U(t)]$ (see Appendix D).

The voltage pulse $U(t)$ is defined according to the steps (i) - (v) of the sequence defined in the main text [see also Fig. 2(a)] as

$$U(t) = \begin{cases} U_i, & \text{for } t < t_0, \\ U_i + \Delta U \cdot g_{\text{lead}}(t), & \text{for } t_0 \leq t < t_s, \\ U_f, & \text{for } t_s \leq t < t_f, \\ U_f - \Delta \bar{U} \cdot g_{\text{trail}}(t), & \text{for } t_f \leq t < t_r, \\ U_r, & \text{for } t \geq t_r. \end{cases} \quad (\text{F2})$$

Here, U_i , U_f , and U_r are the initial, final, and readout voltages, respectively [see Fig. 2 (a)]. The voltage differences $\Delta U = U_f - U_i$ and $\Delta \bar{U} = U_f - U_r$ are chosen to differ to allow the readout mode to decay for the ringdown measurement (see main text for more details). The times t_0 , t_s , t_f , and t_r are chosen such that $t_s - t_0 = t_r - t_f$.

To find a non-adiabatic frequency-sweep that prepares with high-fidelity the sensing state, we rely on the Magnus-based strategy for control [52, 53] as described in Ref. [23] (and Supplemental Material section III of thereof). The first step consists in choosing a first frequency-sweep (the soft ramp introduced in the main text), and which will then be modified by a correcting pulse. The generic form of the corrected ramp is then given by

$$g_a(t) = g_{a,\text{soft}}(t) + g_{a,\text{corr}}(t), \quad (\text{F3})$$

with $a \in \{\text{lead, trail}\}$. Here, we choose the leading edge of the soft ramp to be given by [see Fig. 2 (a) of the main text]

$$g_{\text{lead,soft}}(t) = \frac{1}{2} \left[1 - \cos \left(\pi \frac{t - t_0}{t_s - t_0} \right) \right] \quad (\text{F4})$$

and the correcting sweep is parametrized as

$$g_{\text{lead,corr}}(t) = g_{\text{lead,even}}(t) + g_{\text{lead,odd}}(t) \quad (\text{F5})$$

with

$$\begin{aligned} g_{\text{lead,even}}(t) &= c \left[1 - \cos \left(2\pi \frac{t - t_0}{t_s - t_0} \right) \right], \\ g_{\text{lead,odd}}(t) &= d \left[\sin \left(2\pi \frac{t - t_0}{t_s - t_0} \right) \right], \end{aligned} \quad (\text{F6})$$

where c and d are the free Fourier coefficients that allow one to tune the correcting sweep to cancel transitions to the out-of-plane (OOP) mode. These coefficients are found using the Magnus-based strategy for control as described in the Supplemental Material of Ref. [23].

We can relate the trailing edge to the leading edge of the non-adiabatic detuning-sweep via the relation

$$g_{\text{trail,soft}}(t) = 1 - g_{\text{lead,soft}}(t), \quad (\text{F7})$$

which we then use to find the coefficients \bar{c} and \bar{d} for the trailing edge correcting sweep [see Eqs. (F2) and (F6)]. Since $\Delta U \neq \Delta \bar{U}$ there is no symmetry relation between the coefficients c (d) and \bar{c} (\bar{d}). Note that this arises from the technical implementation of the experiment as discussed in the main text, and it is not a limitation of IAS [23].

Appendix G: Nanomechanical string resonator as a sensor

To validate the sensing capability of the nanomechanical string resonator, we perform finite element simulations using COMSOL Multiphysics to study the effect of electrostatic fields on the mechanical eigenfrequencies. To this end, we add two adjacent electrodes to the model of the string described in Sec. A. To reproduce the dielectric tuning of our sample [27] [c.f. Figs. 1 (c) and S2], we mimick the nominal layout of the sample summarized in Tab. I.

Parameter	Symbol	Current device
Length	L	55 μm
Width	w	250 nm
Thickness	t	100 nm
Electrode width	W	1 μm
Electrode separation	S	$\lesssim 500$ nm
Electrode asymmetry	A	unknown

Table I. **Geometric parameters of the nanostring resonator.** The true electrode geometry, especially the gap between the two electrodes S as well as the exact position of the nanostring determining the asymmetry of the capacitor A , is not precisely known.

We apply a DC bias between the electrode to expose the string to an electrostatic gradient field and perform an eigenfrequency analysis to assess the dielectric frequency shift of the OOP and IP modes. Figure S7 (a) shows the tuning behavior of both modes as the DC bias is swept from 0 V to -12 V. The quadratic tuning behavior of both modes is apparent, reproducing the expected softening (stiffening) behavior of the IP (OOP) mode, respectively [27, 30].

Close to $V_{DC} = -8$ V the avoided crossing clearly emerges as a result of the dielectric coupling between the two modes [27], yielding a splitting $\Omega_0/(2\pi) = 36$ kHz.

Besides the applied DC voltage, the microwave tone applied to the 3D microwave cavity for readout (c.f. Appendix. C) also induces an effective DC voltage, arising from the root-mean-square (RMS) of the microwave field [30]. We also account for the RMS microwave field in the COMSOL simulation. For the sake of simplicity, we describe its effect by adding a net charge density to the dielectric material of the beam, rather than adding the microwave cavity to the model. Figure S7 (b) displays the original DC bias sweep from Fig. S7 (a) (charge density 0 C/m⁻³, blue trace) along with two other charge configurations (charge density 400 C/m⁻³ and 800 C/m⁻³, orange and green trace, respectively) in the region around the avoided level crossing. Clearly, the added charge density impacts the frequency tuning behavior. In Fig. S7 (c), we plot the frequency difference between both branches $\Delta\omega$ for the three charging configurations. Each curve yields a distinct minimum, which heralds the position of the avoided crossing. The minimal value of $\Delta\omega$ corresponds to the splitting Ω_0 . Figure S7 (c) makes it immediately apparent that both the position and the magnitude of the avoided crossing shift with increasing charge density. Figure S7 (d) depicts the dependence of the level splitting Ω_0 on the charge density. The splitting is found to increase almost linearly with the charge density. The COMSOL simulation thus demonstrates a distinct effect of the charge density on the coupling strength between the two mechanical modes.

This is verified in the experiment discussed in the main text (c.f. Fig. 5), where the RMS of the microwave field is used to change the electrostatic environment sensed by the nanomechanical string resonator. This constitutes a proof-of-principle demonstration of the sensing capabilities of the nanomechanical resonator.

For a more quantitative analysis, we start from the theory precision that IAS is expected to resolve changes of order $10^{-4}\Omega_0$, depending on the coherence time of the nanostring (see Fig. 3 of Ref. [23]). This can be conveniently expressed in terms of a net charge density on the nanostring. Based on the slope of Fig. S7 (d), we expect a charge sensitivity of approximately 26 Hz/(C/m³). The shift recorded in Fig. 5 (b) thus corresponds to a charge density of 180 C/m³ or an equivalent of 1,400 electrons added to the nanostring, comparable to other vibrating room-temperature charge sensors [54]. Using the estimated sensitivity of IAS [23] of $10^{-4}\Omega_0$ the charge sensitivity gives rise a minimum detectable charge of 5.65 C/m³, corresponding to approximately 43 electrons on the nanostring. We envision that a series of straightforward improvements of the sample geometry, including a narrower nanostring cross-section as well as a reduced electrode separation, will allow to detect a single electron being added to the nanostring.

A key feature of this sensing scheme is its high time resolution. For the experiment described in the main text [$n = 4$ Ramsey fringes, $m = 8$ iterations, see Fig. 4 (c)], an estimate for Ω_0 is obtained after approximately 1 s. Reducing the number of iterations (see Fig. 5), and taking advantage of an FPGA to apply pre-configured pulses, will allow to reduce the measurement time to a few 100 μ s. This is considerably faster than the comparably sensitive scheme for room temperature charge sensing based on coupled nonlinear mechanical resonators [11] or a single diamond spin [55].

Another potential field of application of IAS vectorial scanning force sensing based on a vibrating nanowire [24–26, 56–58]. The vectorial scanning force sensor is a nanomechanical two-mode sensor. It probes the effect of its electrostatic environment through a change of the splitting between the two normal modes in the coupled reference frame of the nanowire, and thus relies on the same detection principle as IAS. The integration of IAS is therefore straightforward. It promises to increase the sensitivity as a result of its robustness to noisy environments.

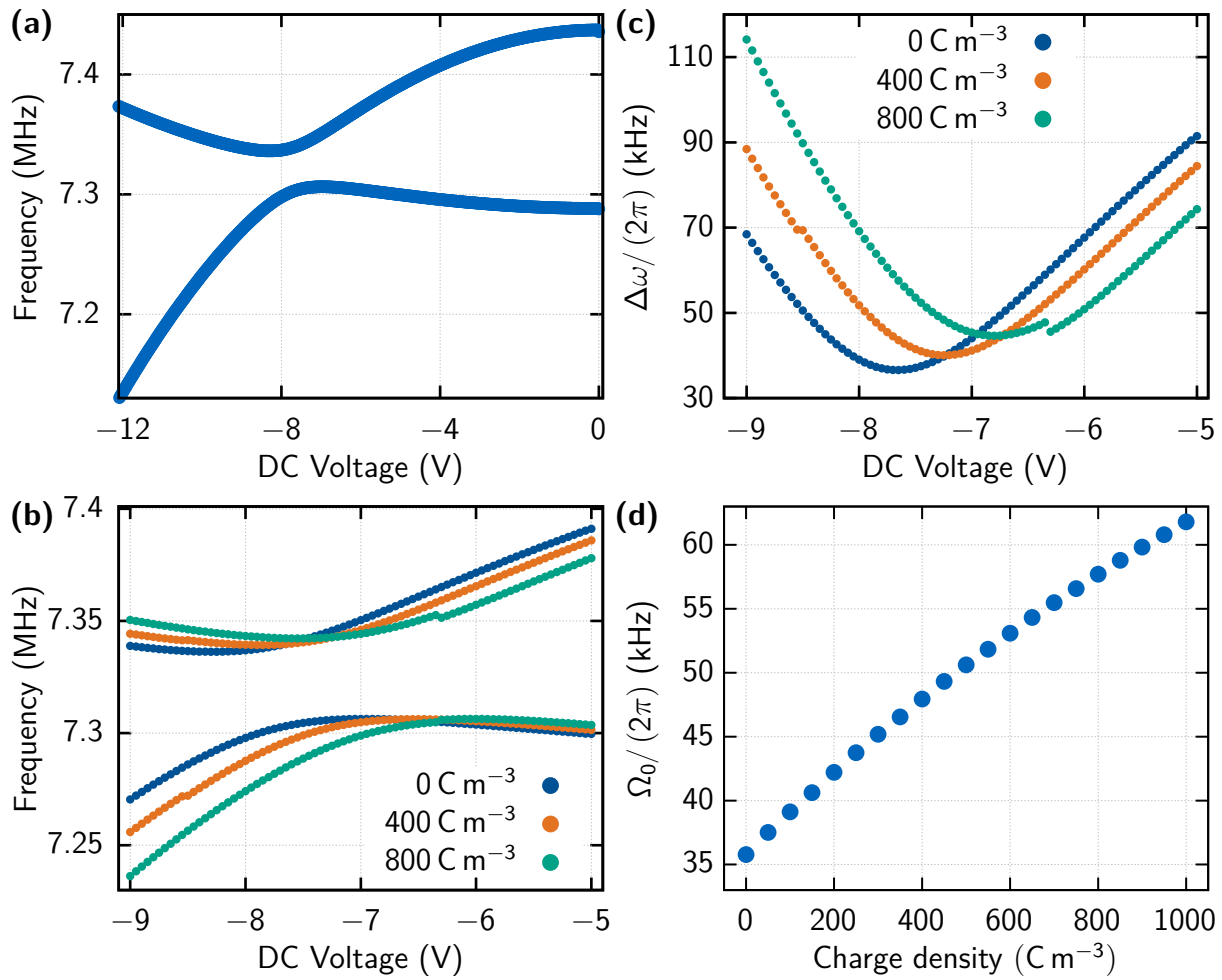


Figure S7. **COMSOL Multiphysics simulation of the dielectric eigenfrequency tuning of the nanomechanical string resonator.** (a) Eigenfrequency tuning of the fundamental IP and OOP flexural mode as a function of an applied DC bias voltage. (b) Closeup in the vicinity of the avoided crossing for three different charge densities on the nanostring, mimicking different RMS microwave fields (0 C/m^{-3} , 400 C/m^{-3} , 800 C/m^{-3} in blue, orange and green, respectively). (c) Frequency difference $\Delta\omega$ between the two branches in (b) for the same three charge densities. (d) Level splitting Ω_0 corresponding to the minimum in (c) as a function of the charge density in the string.